

Subcellular chemical and morphological analysis by stimulated Raman scattering microscopy and image analysis techniques

Annalisa D'Arco,^{1,2} Nadia Brancati,³ Maria Antonietta Ferrara,¹ Maurizio Indolfi,¹ Maria Frucci,³ and Luigi Sirleto^{1,*}

¹National Research Council (CNR), Institute for Microelectronics and Microsystems, I-80131 Napoli, Italy

²Second University of Naples (SUN), Department of Information Engineering, I-81031 Aversa, Italy

³National Research Council (CNR), Institute for High-Performance Computing and Networking, I-80131 Napoli, Italy

*luigi.sirleto@cnr.it

Abstract: The visualization of heterogeneous morphology, segmentation and quantification of image features is a crucial point for nonlinear optics microscopy applications, spanning from imaging of living cells or tissues to biomedical diagnostic. In this paper, a methodology combining stimulated Raman scattering microscopy and image analysis technique is presented. The basic idea is to join the potential of vibrational contrast of stimulated Raman scattering and the strength of imaging analysis technique in order to delineate subcellular morphology with chemical specificity. Validation tests on label free imaging of polystyrene-beads and of adipocyte cells are reported and discussed.

©2016 Optical Society of America

OCIS codes: (190.5890) Scattering, stimulated; (190.7110) Ultrafast nonlinear optics; (180.4315) Nonlinear microscopy; (170.0110) Imaging systems; (100.0100) Image processing.

References and links

1. W. Min, C. W. Freudiger, S. Lu, and X. S. Xie, "Coherent nonlinear optical imaging: beyond fluorescence microscopy," *Annu. Rev. Phys. Chem.* **62**(1), 507–530 (2011).
2. A. M. Streets, A. Li, T. Chen, and Y. Huang, "Imaging without fluorescence: nonlinear optical microscopy for quantitative cellular imaging," *Anal. Chem.* **86**(17), 8506–8513 (2014).
3. R. H. Webb, "Confocal optical microscopy," *Rep. Prog. Phys.* **59**(3), 427–471 (1996).
4. J. A. Conchello and J. W. Lichtman, "Optical sectioning microscopy," *Nat. Methods* **2**(12), 920–931 (2005).
5. W. R. Zipfel, R. M. Williams, and W. W. Webb, "Nonlinear magic: multiphoton microscopy in the biosciences," *Nat. Biotechnol.* **21**(11), 1369–1377 (2003).
6. E. E. Hoover and J. A. Squier, "Advances in multiphoton microscopy technology," *Nat. Photonics* **7**(2), 93–101 (2013).
7. S. Keren, C. Zavaleta, Z. Cheng, A. de la Zerda, O. Gheysens, and S. S. Gambhir, "Noninvasive molecular imaging of small living subjects using Raman spectroscopy," *Proc. Natl. Acad. Sci. U.S.A.* **105**(15), 5844–5849 (2008).
8. M. Li, J. Xu, M. Romero-Gonzalez, S. A. Banwart, and W. E. Huang, "Single cell Raman spectroscopy for cell sorting and imaging," *Curr. Opin. Biotechnol.* **23**(1), 56–63 (2012).
9. J. X. Cheng and X. S. Xie, "Vibrational spectroscopic imaging of living systems: An emerging platform for biology and medicine," *Science* **350**(6250), 62–64 (2015).
10. C. H. Camp, Jr. and M. T. Cicerone, "Chemically sensitive bioimaging with coherent Raman scattering," *Nat. Photonics* **9**, 295–305 (2015).
11. A. Alfonso-García, R. Mittal, E. S. Lee, and E. O. Potma, "Biological imaging with coherent Raman scattering microscopy: a tutorial," *J. Biomed. Opt.* **19**(7), 071407 (2014).
12. A. Zumbusch, W. Langbein, and P. Borri, "Nonlinear vibrational microscopy applied to lipid biology," *Prog. Lipid Res.* **52**(4), 615–632 (2013).
13. E. Ploetz, S. Laimgruber, S. Berner, W. Zinth, and P. Gilch, "Femtosecond stimulated Raman microscopy," *Appl. Phys. B* **87**(3), 389–393 (2007).
14. C. W. Freudiger, W. Min, B. G. Saar, S. Lu, G. R. Holtom, C. He, J. C. Tsai, J. X. Kang, and X. S. Xie, "Label-free biomedical imaging with high sensitivity by stimulated Raman scattering microscopy," *Science* **322**(5909), 1857–1861 (2008).
15. Y. Ozeki, F. Dake, S. Kajiyama, K. Fukui, and K. Itoh, "Analysis and experimental assessment of the sensitivity of stimulated Raman scattering microscopy," *Opt. Express* **17**(5), 3651–3658 (2009).

16. P. Nandakumar, A. Kovalev, and A. Volkmer, "Vibrational imaging based on stimulated Raman scattering microscopy," *New J. Phys.* **11**(3), 033026 (2009).
17. D. Zhang, M. N. Slipchenko, and J. X. Cheng, "Highly sensitive vibrational imaging by femtosecond pulse stimulated Raman loss," *J. Phys. Chem. Lett.* **2**(11), 1248–1253 (2011).
18. D. Fu, G. Holtom, C. Freudiger, X. Zhang, and X. S. Xie, "Hyperspectral imaging with stimulated Raman scattering by chirped femtosecond lasers," *J. Phys. Chem. B* **117**(16), 4634–4640 (2013).
19. M. Ji, D. A. Orringer, C. W. Freudiger, S. Ramkissoon, X. Liu, D. Lau, A. J. Golby, I. Norton, M. Hayashi, N. Y. R. Agar, G. S. Young, C. Spino, S. Santagata, S. Camelo-Piragua, K. L. Ligon, O. Sagher, and X. S. Xie, "Rapid, label-free detection of brain tumors with stimulated Raman scattering microscopy," *Sci. Transl. Med.* **5**(201), 201ra119 (2013).
20. M. Ji, S. Lewis, S. Camelo-Piragua, S. H. Ramkissoon, M. Snuderl, S. Veneti, A. Fisher-Hubbard, M. Garrard, D. Fu, A. C. Wang, J. A. Heth, C. O. Maher, N. Sanai, T. D. Johnson, C. W. Freudiger, O. Sagher, X. S. Xie, and D. A. Orringer, "Detection of human brain tumor infiltration with quantitative stimulated Raman scattering microscopy," *Sci. Transl. Med.* **7**(309), 309ra163 (2015).
21. D. Zhang, P. Wang, M. N. Slipchenko, D. Ben-Amotz, A. M. Weiner, and J. X. Cheng, "Quantitative vibrational imaging by hyperspectral stimulated Raman scattering microscopy and multivariate curve resolution analysis," *Anal. Chem.* **85**(1), 98–106 (2013).
22. D. Fu and X. S. Xie, "Reliable cell segmentation based on spectral phasor analysis of hyperspectral stimulated Raman scattering imaging data," *Anal. Chem.* **86**(9), 4115–4119 (2014).
23. A. Owyong, "Coherent Raman gain spectroscopy using CW laser sources," *IEEE J. Quantum Electron. QE* **14**(3), 192–203 (1978).
24. L. Sirteto, M. A. Ferrara, T. Nikitin, S. Novikov, and L. Khriachtchev, "Giant Raman gain in silicon nanocrystals," *Nat. Commun.* **3**, 1220 (2012).
25. M. A. Ferrara, L. Sirteto, G. Nicotra, C. Spinella, and I. Rendina, "Enhanced gain coefficient in Raman amplifier based on silicon nanocomposites," *Phot. Nano. Fund. Appl.* **9**(1), 1–7 (2011).
26. B. F. Levine, C. V. Shank, and J. P. Heritage, "Surface vibrational spectroscopy using stimulated Raman scattering," *IEEE J. Quantum Electron.* **15**(12), 1418–1432 (1979).
27. J. P. Heritage and D. L. Allara, "Surface picosecond Raman gain spectra of a molecular monolayer," *Chem. Phys. Lett.* **74**(3), 507–510 (1980).
28. K. I. Popov, A. F. Pegoraro, A. Stolow, and L. Ramunno, "Image formation in CARS and SRS: effect of an inhomogeneous nonresonant background medium," *Opt. Lett.* **37**(4), 473–475 (2012).
29. C. Y. Chung, J. Hsu, S. Mukamel, and E. O. Potma, "Controlling stimulated coherent spectroscopy and microscopy by a position-dependent phase," *Phys. Rev. A* **87**(3), 033833 (2013).
30. M. Sezgin and B. Sankur, "Survey over image thresholding techniques and quantitative performance evaluation," *J. Electron. Imaging* **13**(1), 146–168 (2004).
31. M. Frucci, "Oversegmentation reduction by flooding regions and digging watershed lines," *Int. J. Pattern Recogn.* **20**(1), 15–38 (2006).
32. T. R. Jones, A. Carpenter, and P. Golland, "Voronoi-based segmentation of cells on image manifolds," in *Computer Vision for Biomedical Image Applications*, Y. Liu, T. Jiang, and C. Zhang, eds. (Springer, 2005), pp. 535–543.
33. V. Luc and P. Soille, "Watersheds in digital spaces: an efficient algorithm based on immersion simulations," *IEEE Trans. Pattern Anal. Mach. Intell.* **6**, 583–598 (1991).
34. L. Ping-Sung, T. S. Chen, and P. C. Chung, "A fast algorithm for multilevel thresholding," *J. Inf. Sci. Eng.* **17**(5), 713–727 (2001).
35. N. Otsu, "A threshold selection method from gray-level histograms," *Automatica* **11**, 285–296 (1975).
36. M. Frucci, C. Arcelli, and G. Sanniti Di Baja, "On the hierarchical assignment to the foreground of gray-level image subsets," *Int. J. Pattern Recogn.* **20**(06), 897–912 (2006).
37. N. Brancati, M. Frucci, and G. Sanniti di Baja, "Image segmentation via iterative histogram thresholding and morphological features analysis," in *Image Analysis and Recognition*, A. Campilho, and M. Kamel, eds. (Springer, 2008), pp. 132–141.
38. J. Serra, *Image Analysis and Mathematical Morphology* (Academic, 1983).
39. M. Suzuki, Y. Shinohara, Y. Ohsaki, and T. Fujimoto, "Lipid droplets: size matters," *J. Electron Microsc.* (Tokyo) **60**(1 Suppl 1), S101–S116 (2011).
40. V. Rizzatti, F. Boschi, M. Pedrotti, E. Zoico, A. Sbarbati, and M. Zamboni, "Lipid droplets characterization in adipocyte differentiated 3T3-L1 cells: size and optical density distribution," *Eur. J. Histochem.* **57**(3), e24 (2013).
41. S. Fukumoto and T. Fujimoto, "Deformation of lipid droplets in fixed samples," *Histochem. Cell Biol.* **118**(5), 423–428 (2002).
42. Y. Ohsaki, Y. Shinohara, M. Suzuki, and T. Fujimoto, "A pitfall in using BODIPY dyes to label lipid droplets for fluorescence microscopy," *Histochem. Cell Biol.* **133**(4), 477–480 (2010).

1. Introduction

A subject of wide interest in the physical and life sciences is the noninvasive characterization of microscopic objects within a complex heterogeneous system through nonlinear optical

microscopy [1]. Over the past decades, most of our knowledge about cell functions was derived from biochemical assays, which lack the capability of single cell analysis. Therefore, the basic aim of nonlinear microscopy is to perform single cell analysis, in order to enable the characterization of cellular systems with a level of detail that cannot be achieved with ensemble measurements [2].

Quantitative image analysis is fundamental for nonlinear microscopy and, of course, for stimulated Raman scattering (SRS) microscopy, too. The basic idea is that images of cells tend to give only an intuitive understanding of the structure and the spatial distributions of chemicals and organelles, while identification and quantification of such parameters are necessary in order to accurately compare images and make objective conclusions about an experiment. This is crucial for a number of applications spanning from imaging of living cells or tissues until biomedical diagnostic [2].

Computational approaches to bioimaging analysis are increasingly used to extract quantitative information about both the structure and dynamics of biological systems at the single-cell level. On this line of argument, recently, there has been a sudden increase in applications of quantitative biological imaging, a field that has been advanced by developments in optical imaging technology as well as in computational image analysis techniques [2].

Confocal [3,4] and multiphoton fluorescence microscopy [5,6] are important and powerful techniques for imaging of biological samples. However, these microscopic techniques show some limitations. Indeed, they require chemical labels that could interfere with biological functionalities; additionally, the photo-bleaching can introduce artefacts and limit the measurement repeatability. Therefore, it is desirable to implement real-time, three-dimensional imaging with high spatial resolution, high sensitivity, and high chemical selectivity of unlabeled living cells.

Raman microscopy can be used as a contrast mechanism based on vibrational properties. A typical Raman spectrum makes available information on the molecular and chemical structure of the sample, offering an intrinsic chemical selectivity. Nevertheless, linear Raman microscopy is limited to weak signals and the images acquisition times are very long [7,8].

Coherent Raman Scattering (CRS) techniques are sensitive to the same molecular vibrations probed in spontaneous Raman spectroscopy, but unlike linear Raman spectroscopy, CRS techniques exhibit a nonlinear dependence on the incoming light fields and produce coherent radiation. In CRS, the two excitation beams are usually referred as pump and Stokes. When the difference in frequencies is resonant to a molecular vibration, a stimulated and coherent excitation of molecular bond vibration modes (third order non-linear process) occurs and a significant increase of Raman signal is obtained. Therefore, CRS microscopy makes possible to achieve images faster than conventional Raman microscopes [9–12].

So far, most CRS applications have been aimed at label-free imaging of lipids in a variety of samples from artificial model systems, to living cells and tissues. This prevalence is due to the important role of lipids in biology and to favorable signal strengths in CRS experiments. CRS microscopy can help to solve many open questions on lipid-related processes inside cells and tissues, which due to the limitations and artifacts associated with fluorescence lipid staining have been left open [12].

The recent development of SRS microscopy overcame coherent anti-Stokes Raman scattering (CARS) limitations and it provides better imaging mechanism (vibrational) contrast. SRS eliminates the non-resonant background problem, because the generated third order SRS nonlinear polarization is directly heterodyne mixed and amplified by the input beam with the exact same phase, therefore always resulting in a zero non-resonant contribution. In addition, SRS exhibits an identical spectrum as the spontaneous Raman and SRS signal is linearly proportional to the concentration of the analyte, allowing straightforward quantification [13–18].

In [19], Ji et al. described the use of (SRS) microscopy for differentiating healthy mouse brain tissue from tumor-infiltrated brain based on histoarchitectural and biochemical differences, while in [20], Ji et al. show that SRS reveals human brain tumor infiltration in fresh, unprocessed surgical specimens from a number of neurosurgical patients.

In [21], quantitative vibrational imaging by SRS microscopy was presented. SRS images were analyzed by a multivariate curve resolution (MCR) method to reconstruct quantitative concentration images for each individual component and to retrieve the corresponding vibrational Raman spectra. Using these methods, they demonstrate quantitative mapping i.e. maps of principal chemical components along with their respective vibrational spectra were generated. The merit of this method is to provide spatial locations of the analyte inside the cells based on their concentration, but no indications about their morphology can be obtained. In [22], Fu et al. demonstrate spectral phasor analysis method that allows to distinguish many different subcellular components. They obtain the spatial distribution of subcellular components, but no quantification of any subcellular components was reported. At least in our knowledge, for SRS microscopy, this is the first time that in single cell the morphology of subcellular components of the order of a few microns are automatically detected and quantified. This aspect represents the novelty of the paper and the uniqueness of the presented method.

In this paper, a methodology for delineating subcellular morphology with chemical specificity, combining SRS microscopy and image analysis technique, is presented. The paper is organized as follows: in paragraph 2 the details of SRS microscopy implementation and basic ideas about quantitative biological imaging are described; in paragraph 3, quantitative SRS microscopy based on 2D imaging technique is reported and discussed. Finally the conclusions.

2. Methodology

In the field of laser spectroscopy, SRS was extensively studied as a highly sensitive tool of vibrational spectroscopy [23–25]. An important issue is its sensitivity, because the SRS signal is detected as a small change of intensity of the excitation beam, it can be deteriorated by shot-noise and laser intensity noise. It is important to take into account the laser intensity noise, because it can easily surpass the shot noise. The thermal noise can be negligible compared to the shot noise, when the optical power is of the order of a few mW. In order to achieve a shot-noise limited sensitivity for SRS, the basic idea is to take advantage of lock-in high-frequency detection scheme [23–27]. In this approach, to detect the signal, a high-frequency modulation transfer method is used. The intensity of the pump beam is modulated with an electro-optic modulator and the modulation transfer to the probe beam is measured with a lock-in amplifier (LIA), after blocking the pump beam with an optical filter. It is preferable to increase the modulation frequencies, because the relative intensity noise of laser pulses typically decreases with frequency. Increasing modulation frequency of the beam, at frequencies above 1 MHz, it allows to reach the intrinsic limit of photodetectors (PDs) [23–27].

In this paper, SRS microscope, based on femtosecond laser sources, is implemented. Figure 1 shows the schematic layout of the microscope.

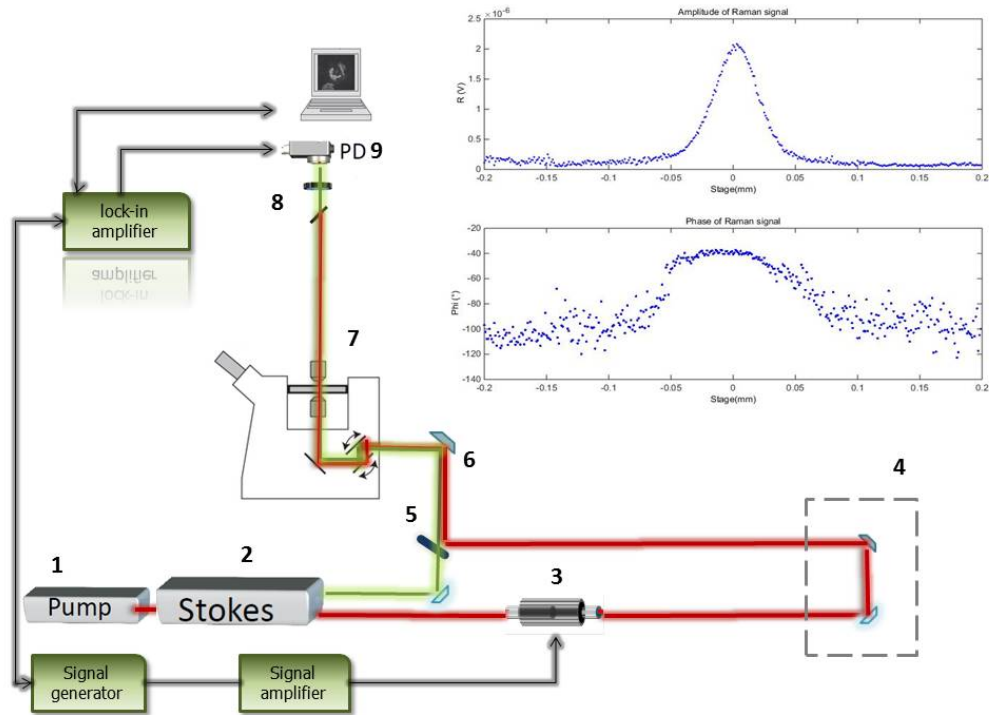


Fig. 1. Schematic layout of SRS microscope: 1. Femtosecond Ti:Sa laser, 2. Synchronized Optical Parameter Oscillator, 3. Pockels cell, 4. Delay line, 5. Dichroic filters, 6. Mirror, 7. Laser scanning microscope, 8. Filters, 9. Detector. Inset in Fig. 1: amplitude and phase of SRS signal measured by LIA.

In our experimental set up, we have two sources. The first one, used as a pump beam, is a fs Ti:Sa laser (Chameleon Ultra II) with a pulse duration of approximately 100 fs, a repetition rate of 80 MHz and emission wavelengths into the range 680-1080 nm. The second one, used as probe beam, is a fs synchronized optical parametric oscillator (Chameleon Compact OPO), pumped by the fs Ti:Sa laser. The OPO has a pulse duration of approximately 200 fs and a repetition rate of 80 MHz, it emits into the range of wavelengths from 1000 to 1600 nm. Due to the possible combinations of Ti:Sa and OPO wavelengths, we investigate the CH-stretching range of the vibrational spectrum (2800 to 3050 cm^{-1}). It is well known that SRS signal can be improved by one order of magnitude when fs pulses are used with respect to ps pulses. In addition, when fs pulses are used, the loss in spectral selectivity of SRS signal is not prejudicial when imaging lipids in the broad spectral range of CH bond vibrations [17].

In order to modulate the pump pulses amplitude, an electro-optic modulator (EOM 350-160 KD*P CONOPTICS) was used, working at a modulation frequency of 4.5 MHz. The Ti:Sa and OPO beams were collinearly combined by a dichroic mirror (Semrock FF875-Di01-25x36), temporally overlapped by a delay line (Newport MOD M-ILS200CC) and focused inside the sample by a 60X high numerical aperture multiphoton objective (Nikon, Plan Apo IR, NA 1.27). We note that better collection efficiencies are obtained with higher-NA microscope objectives. This is especially important for the SRS techniques, where photothermal and position-dependent interference effects may introduce artifacts in the image [28,29]. Such effects can be mitigated by choosing a high-NA microscope objective. Therefore in our set up, output pulses are collected by a 40X high numerical aperture multiphoton objective (Nikon, Apo 40X, NA 1.25). Afterwards, a stack of optical filter removes the pump pulses, while probe pulses are detected by a PD (Thorlabs DET 10/N

InGaAs). The output current is low-pass filtered (minicircuit BLP -5+) to suppress the strong signal due to the laser pulsing (80 MHz) and terminated with 50 Ω . The filtered current is measured by a high frequency LIA (SR844-200 MHz dual phase).

In the inset of Fig. 1, a measurement of SRS spectroscopy is reported. It was carried out on a single point of a phosphate buffer solution in which polystyrene beads, with a diameter of 3 μm , are dispersed. The solution is placed inside a sandwich of two coverslips. In order to investigate a typical CH bond of polystyrene (Raman shift of 3054 cm^{-1}), the pump signal was set to 809 nm with a focused power of 8 mW, while the probe signal was set to 1073 nm with a focused power of 8 mW. The temporal overlap of these two beams was obtained by scanning the delay line with steps of 0.001 mm corresponding to 13.3 fs time-shift. The time constant of the LIA was set to 3 ms with a slope of 18 dB/oct and 10 μV sensitivity. The measured values from LIA, in terms of phase and amplitude of SRS signal as a function of the probe-pump delay in ps, are reported in inset of Fig. 1. The maximum value of SRS signal is obtained, when the best overlap between the two beams is achieved. In this case, a signal-to-noise ratio (SNR) of 8.3 is obtained.

Because SRS uses near-infrared excitation light, SRS imaging modality shares many of the imaging properties of a multiphoton microscope, including fast image acquisition and sub-micrometer resolution. Schematic diagram of a typical nonlinear optical imaging configuration implemented in a scanning microscope is the following: the excitation light is directed through two scanning mirrors (SM) which raster the focal spot across an X-Y plane within the specimen. At every point, the signal is recorded and used to reconstruct a two-dimensional image of the specimen. Commercial laser-scanning microscopes can be upgraded in SRS imaging modality with some important modification. Basically, SRS microscope can be constructed from a laser-scanning microscope by equipping a non-descanned forward detector with proper bandpass filters and LIA detection scheme.

In our case, SRS spectroscopy set up is integrated in an inverted research microscope (Eclipse TE-2000-E, Nikon) equipped with a fast mirror scanning unit (C2, Nikon). The excitation beams, overlapped in time and space, are directed into the microscope through the mirror scanning unit. After interaction with the sample, the beams are collected by a forward detector inserted in the inverted microscope. 2D image is obtained by synchronizing our forward detection unit with the microscope scanning unit. The synchronization is achieved by managing by PCI card (NI PCIe 6363), the electrical signal from the LIA and the digital signals from microscope scanning unit controller.

One of the primary tasks in quantitative image analysis of single cells, which is often necessary before other procedures can be executed, is image segmentation. The goal in image segmentation is to divide an entire field of view into discrete areas that represent meaningful objects. Additionally segmentation is used to partition organelles and structures within a cell as well. It is worthy of noting that with label-free nonlinear optical imaging, segmentation must be tailored to the intrinsic contrast modality. Therefore, quantitative biological imaging for SRS modality can be achieved not only with an optimization of microscopy apparatus but also with appropriate implementation of image analysis technique.

3. Results and discussion

In this section in order to validate the proposed methodology, two examples are reported and discussed. In the former, label free imaging of polystyrene beads (same sample used in the previous paragraph) is considered, while in the latter, label free imaging of fixed adipocyte cells is carried out. All the images, shown in this paragraph, are single recordings of 512 \times 512 px with dimensions 60 μm \times 60 μm and acquisition time of 16 s. The LIA time constant was set to 100 μs with a slope of 18 dB/oct and a sensitivity of 10 μV .

At the top of Fig. 2(a), the image obtained by linear absorption modality is reported. In this case, a single beam, i.e. the OPO at 1073 nm, is used and the transmitted beam intensity

from the sample is measured by PD and directly acquired by the PCI card. At the bottom of Fig. 2(a) the image obtained by vibrational SRS contrast is reported.

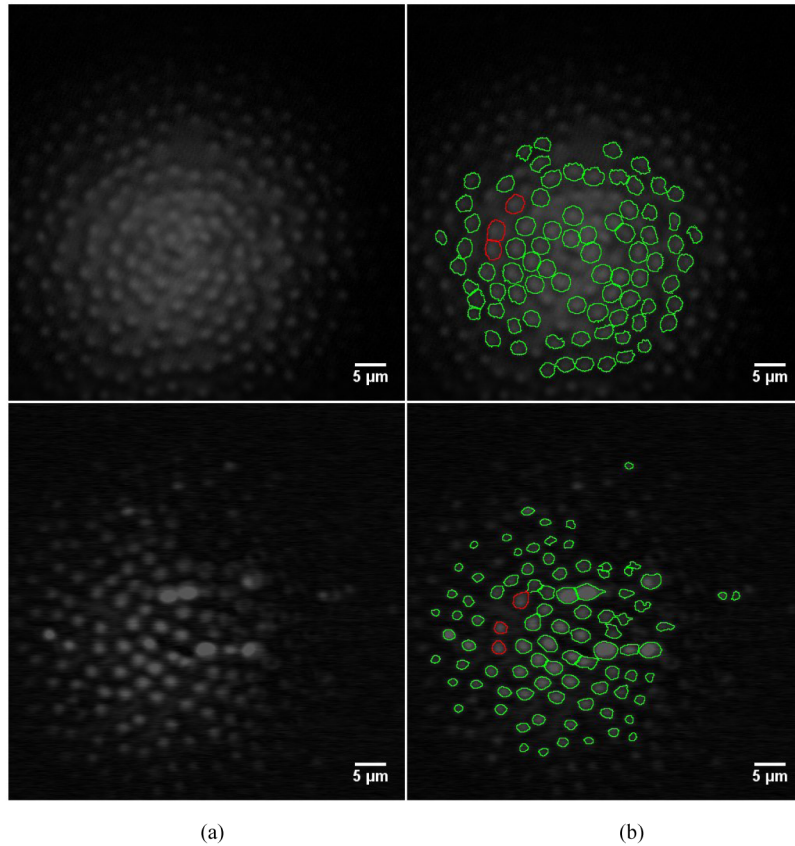


Fig. 2. a) absorption image (top) and SRS image (bottom); b) segmented absorption image (top) and segmented SRS images (bottom).

On both images a process of segmentation is performed. It is applied only on the field of view of the examined image, to avoid the generation of false regions in low contrast areas of the image. Because of the two images have been acquired according to two different modalities and show different intensity and contrast features, a specific segmentation process for each of them have to be applied. Concerning the absorption image, starting from some seeds identified in the lighter areas of the image [30–33], the segmentation process is based on a region growing process, allowing to obtain the contours of the regions at high intensity in gray levels. Concerning SRS image, the segmentation process is based on thresholding techniques (Multi Otsu Threshold Algorithm) [34,35] and on methods for the identification of the contours in correspondence of high intensity variations of the gray levels of the image [36–38]. The main steps of the procedure adopted are listed in Fig. 3 to obtain the segmentation of SRS image.

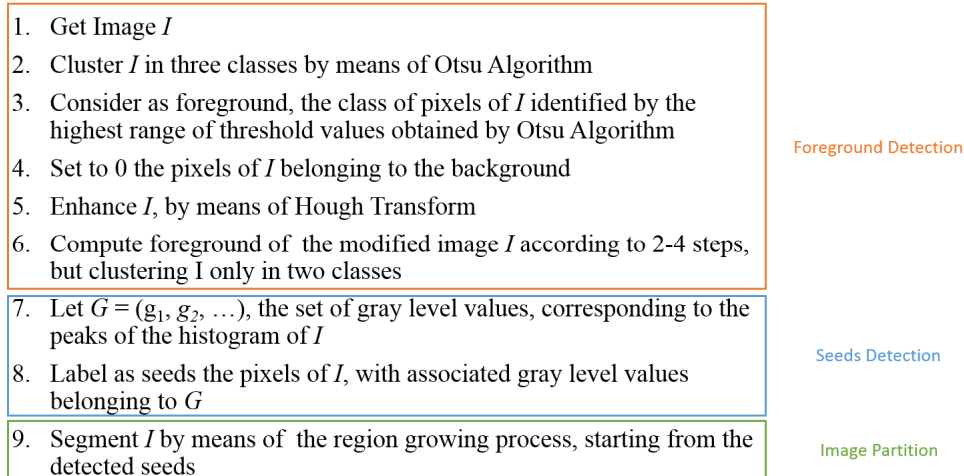


Fig. 3. The procedure for the segmentation of image I obtained by SRS.

In Fig. 2(b), examples of the segmentation process are shown. At the top, the absorption image segmentation, while at the bottom, the SRS image segmentation are, respectively, reported.

As a test for our experimental set up, the temporal delay, introduced by the LIA in SRS image with respect to absorption image has been evaluated. The temporal delay is obtained measuring the spatial shift among the red-contoured regions in the absorption segmented image (top of Fig. 2(b)) and the corresponding red-contoured regions in the SRS segmented image (bottom of Fig. 2(b)). Afterwards the centroids of individuated regions are computed, the spatial shift value is obtained measuring their distance. In order to obtain a more accurate spatial shift measurement, this procedure is repeated for a number of regions and spatial shift value is obtained by averaging the values computed for each step. For the example in Fig. 2(b), taking into account the red contoured regions, the value of spatial shift computed along the x-axis is $(183 \pm 31) \mu\text{s}$.

In Fig. 4(a), polystyrene beads images, obtained changing the objective microscope vertical axis with step of $1 \mu\text{m}$, are reported, indicating the three dimensional sectioning capability of SRS technique.

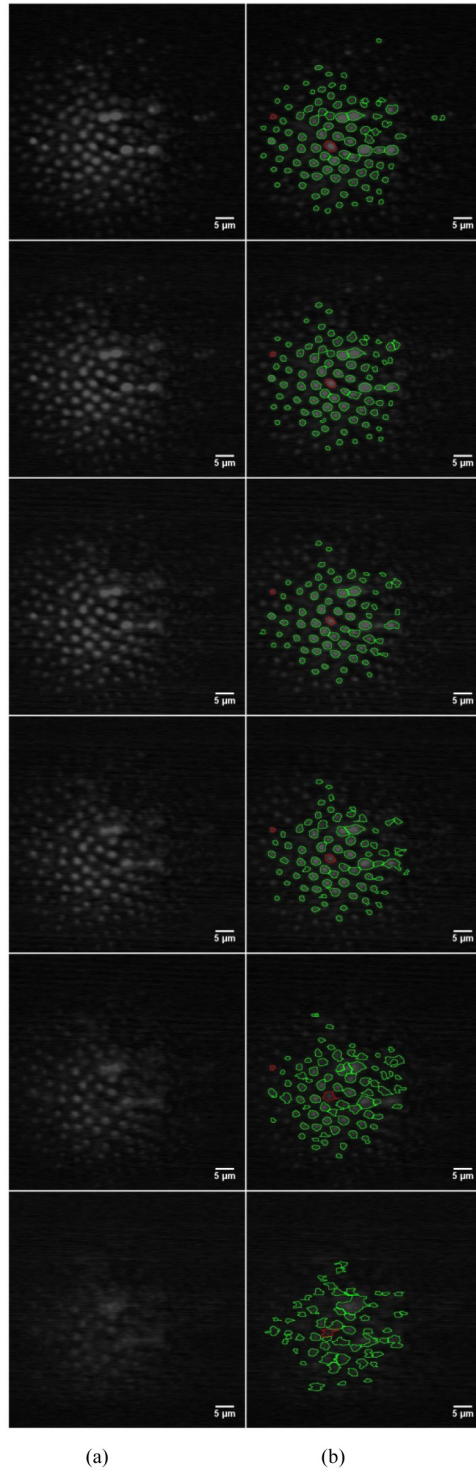


Fig. 4. a) SRS images; b) segmented images: red-contoured regions represent the selected polystyrene-beads for which some features have been computed.

In Fig. 4(b), the results of segmentation process performed on SRS images are shown. In order to evaluate possible morphological changes of the two selected red-contoured regions, some quantitative features as area, eccentricity, major axis, minor axis and average value of gray levels has been computed. The obtained results are summarized in Table 1.

Table 1. Some quantitative measurements of two selected polystyrene-beads. a) results for the left red-contoured region in each image of Fig. 4(b). b) results for the right red-contoured region in each image of Fig. 4(b).

Image	I bead (a)					II bead (b)				
	Intensity Gray levels	Area (μm^2)	Eccentricity	Major Axis (μm)	Minor Axis (μm)	Intensity Gray levels	Area (μm^2)	Eccentricity	Major Axis (μm)	Minor Axis (μm)
Z1	9699	1.5	0.59	1.6	1.3	14942	5.6	0.73	3.2	2.2
Z2	11010	1.3	0.58	1.4	1.2	16593	4.0	0.75	2.8	1.8
Z3	11665	1.1	0.46	1.3	1.1	15925	3.2	0.75	2.5	1.6
Z4	10420	1.2	0.50	1.4	1.2	12190	4.3	0.70	2.8	2.0
Z5	8454	1.4	0.52	1.5	1.2	8454	5.5	0.71	3.3	2.3
Z6	-	-	-	-	-	6881	5.3	0.85	4.0	2.1

We note that the investigated part of sample inside the field of view has a shape of an approximate spherical cap and, while on the border it is possible to individuate some single bead, when we move towards the center, conglomerates of beads are more frequently present. This is evident looking at the top of Fig. 2(a), in which absorption image is reported.

Observing the results in Table 1, concerning the bead (a), which is placed on the border of field of view, we note that the biggest differences between major and minor axis is of about $0.3 \mu\text{m}$. We consider negligible this difference and we conclude that the individuated object is spherical as expected.

In Table 1, concerning bead (b), which is placed at center of field of view, we note that a conglomerate is individuated. In this case the differences between major and minor axis are of about $1 \mu\text{m}$, (with the exception for the quote Z6, for which its value is of about $2 \mu\text{m}$) and we conclude that an elliptical object is individuated. We note that conglomerate is the most challenging case for our algorithm. The low image intensity variations and the low contrast can cause the difference of the individuated shape object with respect to the expected one. However, even if a slightly distortion is observed, we note that the calculated values of minor and major axis are always smaller than the single bead diameter. There are a few exceptions. For quotes Z1 and Z5, the differences between calculated major axis and single bead diameter are 0.2 and $0.3 \mu\text{m}$, respectively. Therefore, we consider negligible these differences, whereas the only significant difference is obtained for the quote Z6 for which its value is about $1 \mu\text{m}$.

SRS has proven to be particularly powerful for studying lipid rich structures. The relatively isolated Raman peaks associated with vibrational states of the CH bond, which are abundant in fatty acid molecules, provide a unique signature for lipids inside a cell. Additionally the densely packed structure of a lipid body (lipid droplets (LDs)) provides an especially strong signal for SRS microscopy. LDs are cellular organelles, participating in a broad variety of physiological processes and are found in many different cell types. Their sizes vary from some tens of nm to tens of μm in diameter [39,40]. A major application of CRS microscopy in quantitative studies of LDs is the monitoring of their numbers and sizes [41,42]. The morphological dynamics of LDs are most striking in adipocytes.

In our example, label free imaging of fixed adipocyte cells are carried out. Selecting a Raman shift of 2845 cm^{-1} and increasing of $1 \mu\text{m}$ the vertical axis of objective microscope, the images reported in Fig. 5(a) have been obtained.

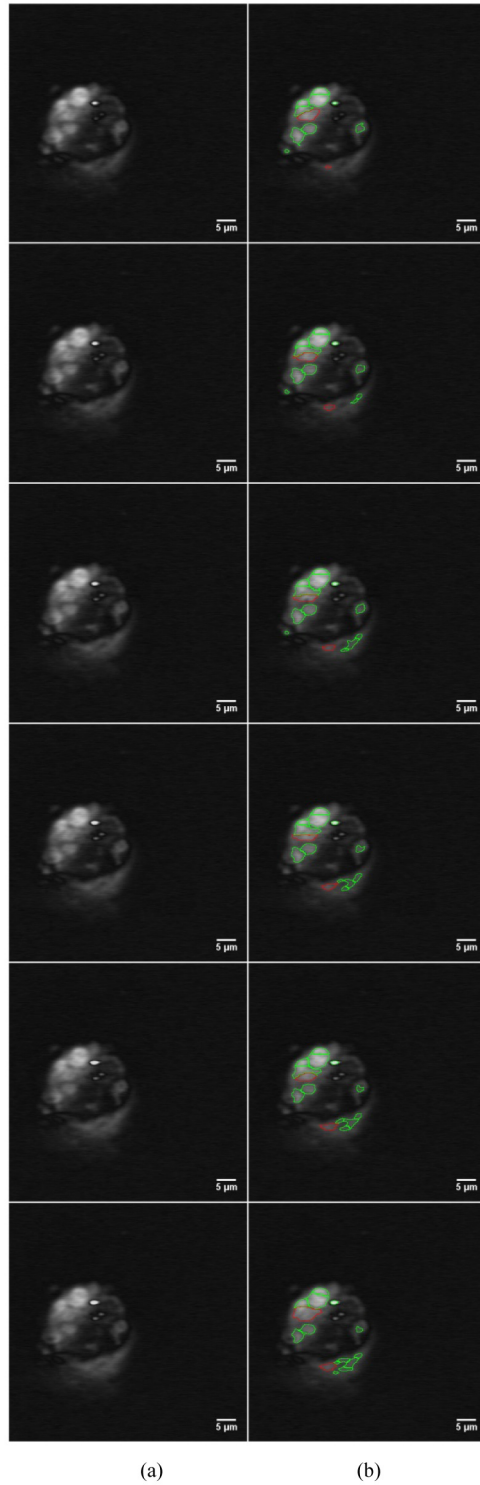


Fig. 5. a) SRS images; b) segmented images: red-contoured regions represent the selected LDs for which some features have been computed.

In Fig. 5(b), the results of segmentation process, performed on SRS label free images of adipocyte, are reported. The quantitative results for two selected LDs (red-contoured regions in Fig. 5(b)) are summarized in the Table 2.

Table 2. Some quantitative measurements of two selected LDs. a) results for the left red-contoured region in each image of Fig. 5(b). b) results for the right red-contoured region in each image of Fig. 5(b).

Image	I lipid droplet (a)					II lipid droplet (b)				
	Intensity Gray levels	Area (μm^2)	Eccentricity	Major Axis (μm)	Minor Axis (μm)	Intensity Gray levels	Area (μm^2)	Eccentricity	Major Axis (μm)	Minor Axis (μm)
Z1	30867	11.9	0.89	5.9	2.7	19529	1.0	0.89	1.6	0.7
Z2	29032	10.1	0.92	5.9	2.3	18677	3.5	0.86	3.0	1.5
Z3	28835	9.2	0.96	6.5	1.9	19529	3.9	0.89	3.4	1.5
Z4	28115	8.5	0.96	6.6	1.8	19267	4.9	0.92	4.2	1.6
Z5	28246	8.1	0.92	5.4	2.1	19464	6.0	0.92	4.6	1.8
Z6	29491	19.8	0.86	7.1	3.7	19661	6.1	0.89	4.2	2.0

Concerning adipocyte cells images, we note that for individuated object no particular shape is expected, since they can blend in a unique three dimensional complex structure. Observing the results in Table 2, concerning the LD (a), we note that the minimum value of differences between major and minor axis is of 3.2 μm , while the maximum value is of 4.6 μm . Concerning the LD (b), the minimum value differences between major and minor axis is of 0.9 μm and the maximum is of 2.8 μm .

Observing the data reported in Table 2, we note a significant changes of some parameters of two selected LDs. For example, concerning LD (a), its area value calculated at Z6 quote is about twofold the one calculated in Z1. Concerning LD (b), its area value calculated at Z6 quote is sixfold the one calculated in Z1. Our findings prove that proposed methodology allows to verify the presence of the LDs inside the cell, to evaluate their morphology, to demonstrate the importance of accurately compare images and to make objective conclusions about an experiment.

4. Conclusions

In this paper, in order to delineate subcellular morphology with chemical specificity, a methodology, based on combination of SRS microscopy and image analysis technique, has been developed and tested on label free imaging of polystyrene-beads and adipocytes. Our findings demonstrate that SRS microscopy combined with a careful evaluation and selection of processing algorithms can lead to an accurate segmentation of LDs inside a single cell.

The proposed methodology is a simple, efficient and robust approach, which could be a multipurpose solution to a number of different biological problems, starting from functional analysis of single living cells to noninvasive diagnosis of human diseases and translational medical imaging applications.

Acknowledgments

We really appreciate Giacomo Cozzi, product specialist from Nikon Instruments, for his continuous support. We thank Vitaliano Tufano from IMM-CNR, for his valuable technical assistance. This work was partially supported by Italian National Operative Programs PONa3_00025 (BIOforIU) and by Euro-bioimaging large scale pan-European research infrastructure project.